

# An Integral Droop for Transient Power Allocation and Output Impedance Shaping of Hybrid Energy Storage System in DC Microgrid

Pengfeng Lin<sup>1</sup>, Student Member, IEEE, Peng Wang<sup>2</sup>, Senior Member, IEEE, Jianfang Xiao, Member, IEEE, Junjun Wang<sup>1</sup>, Student Member, IEEE, Chi Jin, and Yi Tang<sup>1</sup>, Member, IEEE

**Abstract**—Power allocation in hybrid energy storage systems (HESSs) is an important issue for dc microgrids. In this paper, an integral droop (ID), inspired by the electrical characteristics of capacitor charging/discharging process, is proposed and applied to a cluster of energy storages (ESs) with high ramp rates. Through the coordination of the ID and conventional  $V$ - $P$  droop, the transient power allocation in HESSs can be intrinsically realized in a decentralized manner. The high-frequency components of power demand can be compensated by the ESs with ID, whereas the ESs with  $V$ - $P$  droop respond to the smooth change of load power. Additionally, the ID coefficient can be designed according to the nominal ramp rate of the ESs with slow response, which helps to extend the lifespan of the HESS. On the other hand, to easily assess the stability of the system feeding constant power loads, a minimum relative impedance criterion (MRIC) is developed. Based on MRIC, it is revealed that the proposed ID can shape the output impedance of the HESS and stabilize the entire system. The feasibility and effectiveness of ID are verified by both simulations and experimental results.

**Index Terms**—Hybrid energy storage systems (HESSs), integral droop (ID), output impedance shaping, transient power allocation.

## I. INTRODUCTION

INCREASING energy shortage and environmental problems have driven the social efforts to search for alternative energy supplies to displace conventional power sources such as coal, oil, and natural gas [1]. One fair choice is to make full use of distributed energy resources (DERs) powered by clean energy, such as solar photovoltaic (PV), fuel cells, and wind power, and further integrate these DERs into existing electrical power systems. Microgrids (MGs) provide an effective way to interconnect diversified types of DERs and electrical loads [2].

Manuscript received April 14, 2017; revised July 11, 2017; accepted August 14, 2017. Date of publication August 16, 2017; date of current version March 5, 2018. This work was supported by the Energy Research Institute at Nanyang Technological University, Singapore. Recommended for publication by Associate Editor B. Semail. (Corresponding author: Pengfeng Lin.)

P. Lin, J. Xiao, J. Wang, and C. Jin are with the Energy Research Institute, Nanyang Technological University, Singapore, 637141 (e-mail: linp0010@e.ntu.edu.sg; jfxiao@ntu.edu.sg; wangjunjun@ntu.edu.sg; jinchi@ntu.edu.sg).

P. Wang and Y. Tang are with School of Electrical and Electronic Engineering, Nanyang Technological University, Singapore, 639798 (e-mail: epwang@ntu.edu.sg; yitang@ntu.edu.sg).

Color versions of one or more of the figures in this paper are available online at <http://ieeexplore.ieee.org>.

Digital Object Identifier 10.1109/TPEL.2017.2741262

When the MGs are connected to the utility grid, power interactions among DERs, loads, and the grid are induced and the benefits of clean energy can be maximized to realize the optimal operation of MGs. Meanwhile, MGs can also work in islanding mode in the case of utility grid failures, and minimize the unfavorable impact of grid faults.

Normally, MGs can be categorized into alternative current (ac) MGs and direct current (dc) MGs. AC power delivery has played a dominant role in the conventional generation, transmission, and distribution networks for more than a century [3], [4]. This fact leads to the extensive academic studies of ac MGs. Nonetheless, the interest in dc MGs is progressively increasing since many renewable energy sources (RESs), energy storages (ESs) and energy-efficient loads are dc by nature. To incorporate the aforementioned dc electrical components, dc MGs may be a better way to realize less power conversion and higher efficiency compared to its ac counterparts.

In dc MGs, RESs are usually characterized by power fluctuation and intermittency, which challenge the reliable operation of the entire system. The difference between the power generated by RESs and consumption of loads is normally defined as power mismatch [5]. To compensate this power imbalance, energy storages systems (ESSs), serving as the power buffer of MGs, are considered to be a desirable solution. The surplus power produced by RESs can be stored in ESSs, whereas the power will be released by ESSs in the case of overstressed loads. Unfortunately, no single ES is capable of meeting the expectations of both high energy density and high power density. A cluster of ESs with high ramp rate such as supercapacitors (SCs) is featured by high power density but restrained energy density. In contrast, electrochemistry-based ESs, such as lithium-ion batteries, have high energy density but limited power density. Instead of simply increasing the capacity of ESs to meet high power and energy demand, hybrid energy storage systems (HESSs), taking the advantages of different ESs, can provide a more feasible option. It has been broadly implemented in dc MGs.

To optimize the energy management system (EMS) for dc MGs, the hardware configurations regarding HESSs has been comprehensively explored in the literature. They can be classified as passive, semiactive, and active types [6]. Passive coordination directly connects the battery and SC in parallel to power the loads without any controllers [7], [8]. Conceding that

the passive coordination is simple and effective, however, the controllability and flexibility of the entire HESSs are inevitably compromised. The system scalabilities are also adversely constrained due to the limited control degree of freedom. The semiactive coordination only integrates a dc/dc converter to the battery, whereas SC is directly interfaced with the output port of the converter without any interlinking devices. This method takes the advantages of regulating the battery current to a near constant [9]–[11]. However, the semiactive coordination is challenged by the fact that capacitor values would be excessively large because of voltage matching problems. The active coordination is by far universally considered to prevail over the passive and semiactive ones. Through the active coordination, all ESs possess their own local converters to fully achieve power dispatch. Besides, the dynamic responses of ESs with different ramp rates can also be regulated by properly designing the controllers for interfacing converters. In order to flexibly schedule the ESs, active coordination is utilized for HESSs in this paper.

The control algorithms for HESSs based on active coordination can further be categorized as decentralized, centralized, and distributed ones. It is worth noting that both centralized and distributed controls are substantially vulnerable to system communications failures. Model predictive control (MPC) is utilized in a central controller to generate low/high frequency power references for batteries and SCs respectively, as in [12]. In this way, the coordination of HESS is achieved. The similar idea can also be found in [13] where the coordinated operation of diversified ESs is realized in a centralized way. Distributed control requires information exchange between neighboring ESs for evaluating consensus algorithms (CAs) [14]–[16]. However, it should be mentioned that in the case of single-point failures, the operation of centralized and distributed control schemes will be detrimentally influenced, and the whole system would even collapse. Additionally, MPC and CAs will absolutely complicate the controllers because the mathematical operations are computationally demanding. For decentralized control, multiple participating converters are integrated close to the dc bus, the output voltage of each converter, also referred to as a local bus signal, almost equals the dc bus voltage. The converters have the perception of the common bus voltage and further know the status of the others, and consequently no information exchange among converters is required [17], [18]. **In this sense, the system under decentralized control is conceived to be the most reliable one among the three methods. The integral droop (ID), which is proposed for HESSs in this paper, will also be shown to have the benefits of decentralized control.**

To dynamically schedule the power among ESs characterized by different ramp rates, the high pass filters (HPFs) and low pass filters (LPFs) are normally utilized to decouple power demand into high-/low-frequency components. In [19], the HPF and LPF are integrated into local controllers as virtual impedances for dc/dc converters. Whereas in [5], an LPF is applied to the converter voltage feedback loop of ESs with slow dynamics, aiming to allocate low frequency power to them. Regardless of the adoption of HPF and LPF, to further simplify the power decoupling mechanism and retain transient power allocations in HESSs, this paper proposes an ID that is inspired by

investigating the charging/discharging procedures of the capacitors. The ID control is then applied to the ESs with quick responses and high power density, and the conventional *V-P* droop is assigned to the ESs with relatively slow responses. Through the coordinated operations of ID and *V-P* droop, the HPF/LPF for power decomposition can be inherently formulated. When the load step-up/-down is enabled, the ESs regulated by ID can handle the high-frequency power change, whereas ESs with *V-P* droop would respond to low-frequency power demand.

Apart from the transient power allocation issues in HESSs, sufficient system stability margin in the steady state should also be ensured for all possible operating conditions. The dc MG stability is normally challenged by those converters with tightly regulated constant power, such as speed regulated motor drive and electronic loads. Within control bandwidth, these types of converters can be simulated as constant power loads (CPLs), which exhibit negative impedances in low frequency range and threaten system stability. Differently, an ideal CPL has infinite control bandwidth and its input impedance always has phase of  $-180^\circ$  at all frequencies. With no generality lost and considering the worst case, in this paper, the ideal CPL is adopted for all the relevant analyses. A minimum relative impedance criterion (MRIC), which is the simplified version of Nyquist criterion, is derived in this paper especially for a class of systems integrated with CPLs. The output impedances of a system including the ID and the *V-P* droop is compared with the one with only *V-P* droop controllers. Using MRIC, it is shown that the proposed ID controller helps to shape the impedance of HESS and increase the stability margin of the whole system.

Following the introduction given in Section I, the derivation of the ID controller is provided in Section II. The transient power allocation scheme in HESSs is analyzed and the ID coefficient design is also explicated. Section III presents an effective method of a proportional-integral (PI) controller design for localized dc/dc converters by means of pole placement. The functionality of output impedance shaping of HESSs and the system stabilization effect of the proposed ID are also studied. Simulations and experimental verifications are respectively detailed in Sections IV and V. Finally, Section VI draws the conclusion of this paper.

## II. PROPOSED ID AND TRANSIENT POWER ALLOCATION IN HESS

### A. Configuration of DC MG With HESS

A generic schematic of an autonomous dc MG is shown in Fig. 1. A wind turbine and a number of solar PV panels, serving as clean power suppliers, are operated under the maximum power point tracking mode. A diesel generator is employed as the backup generation and linked to the dc bus through an ac/dc power converter. DC resistive loads are directly connected to dc bus, whereas energy conversion devices are needed for ac loads. A motor drive (MD) is generally regarded as a type of CPL due to its tightly regulated load power. The HESS consisting of various ESs is explicitly highlighted in Fig. 1 and they are connected to the common dc bus through bidirectional dc/dc converters to realize either charging or discharging functionality.

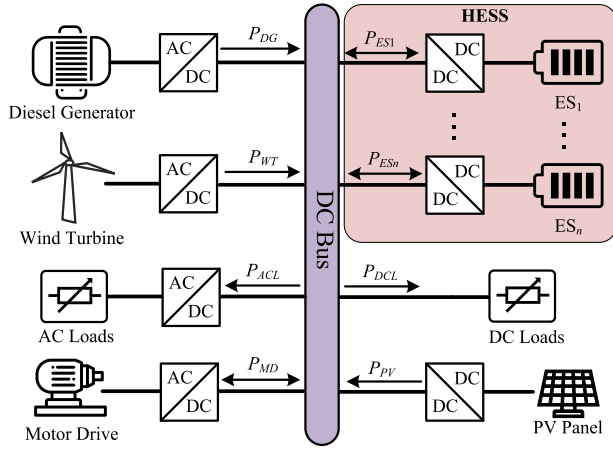


Fig. 1. Generic schematic of an autonomous dc microgrid.

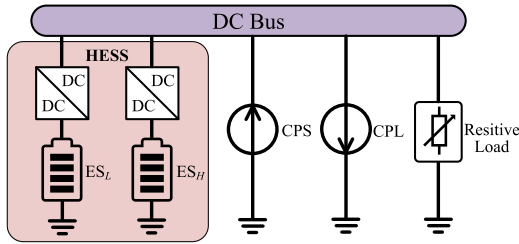


Fig. 2. Simplified schematic of a dc MG integrated with HESS.

As this paper focuses on the overall performances of the HESS, those RESs can be emulated as a lumped constant power source (CPS), and by the same token, the MD, as well as other power electronic loads, are modeled as a lumped CPL [20]. Moreover, for convenient explanation, ESs are classified as a cluster of low ramp rate ESs ( $ES_L$ ) and a cluster of high ramp rate ESs ( $ES_H$ ), respectively. The layout of the entire dc MG can be accordingly simplified, as shown in Fig. 2, which contains HESS, CPS, CPL, and resistive load, respectively.

The power demand  $P_d$  in this paper is defined as the difference between the total power consumption and the CPS as follows:

$$P_d = P_{CPL}(t) + P_R(t) - P_{CPS}(t) \quad (1)$$

where  $P_R(t)$  is the power consumed by the resistive load, as detailed in Fig. 2.  $P_{CPL}(t)$  and  $P_{CPS}(t)$  are the power of CPL and CPS along with time.

It is important to emphasize that the HESS will be discharged if  $P_d$  is positive and charged if it is negative. Under both cases, the fast change of  $P_d$  should be ideally allocated to  $ES_H$  while  $ES_L$  only responds to the slow  $P_d$  change. This helps to prolong the lifetime of HESS. As mentioned earlier, a simple way to realize power allocation is to add HPF/LPF into the control loops of interfacing converters. To further simplify the local controllers and enhance the system reliability, a novel ID for  $ES_H$  to achieve dynamic power sharing will be derived in the subsequent context.

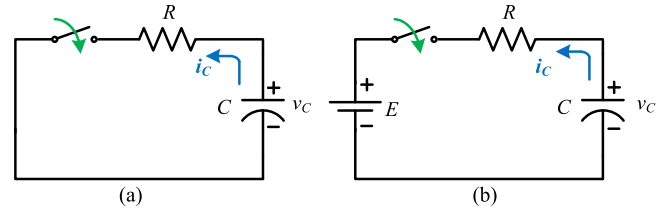


Fig. 3. Illustrative circuits for discharging/charging process of a capacitor. (a) Discharging. (b) Charging.

### B. Integral Droop

It is well known that increasing the capacitance of dc bus will mitigate the bus voltage deviation and contribute the enlarged stability margin to the whole system [21]. A capacitor connected straight to the dc bus will naturally inject/absorb power to/from the bus in the case of load changes. Based on this fact, the electrical characteristics of the capacitor during both charging and discharging processes should be carefully reviewed in order to provide the theoretical basis of the proposed ID control. The illustrative circuit comprising a capacitor in series with a resistor is shown in Fig. 3.

Performing Kirchhoff's voltage law for the discharging case as described in Fig. 3(a), the differential equation of the capacitor is given by

$$RC \frac{dv_C}{dt} + v_C = 0 \quad (2)$$

where  $R$ ,  $C$ , and  $V_C$  represent the series resistance, capacitance, and capacitor voltage, respectively. Solving the dynamic equation (2), the time-domain descriptions of the capacitor voltage and current are obtained given as follows:

$$\begin{cases} v_C = V_0 e^{-t/RC} \\ i_C = \frac{V_0}{R} e^{-t/RC} \end{cases} \quad (3)$$

where  $V_0$  denotes the initial voltage on the capacitor. Accordingly, the mathematical solution for the charging case can also be presented as

$$\begin{cases} v_C = E + (V_0 - E) e^{-t/RC} \\ i_C = \frac{V_0 - E}{R} e^{-t/RC} \end{cases} \quad (4)$$

where  $E$  is the external dc source.  $V_0$  is assumed to be smaller than  $E$ , which means that the capacitor can be charged after switching ON and its voltage will eventually increase to  $E$  in a steady state. Combining (3) and (4), the generalized relation between  $v_C$  and  $i_C$  can be summarized as

$$v_C = V_0 - k \int i_C dt \quad (5)$$

where  $k = 1/C$  is a constant indicating the discharging/charging rate. For both the cases discussed above, the corresponding voltage and current profiles depicted by (3) and (4) are also shown in Fig. 4. It is easily observed that the capacitor tends to supply the burst power at the instant when the switch is ON and the power exponentially decreases to zero at the end of discharging/charging process. The features of capacitor currents illustrated in Fig. 4 give the inspiration to design a new droop

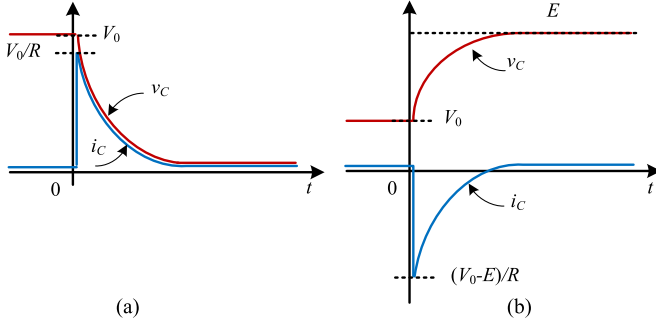


Fig. 4. Profiles of voltage and current of the capacitor during discharging/charging process. (a) Discharging. (b) Charging.

controller, which bears the identical format as (5) by replacing current with power value. The new controller is called ID and is given as follows:

$$V = V_n - n \int P_H dt \quad (6)$$

where  $V_n$  is the nominal voltage reference as in conventional  $V$ - $P$  droop controller,  $n$  is the ID coefficient, which should be carefully tuned in order to obtain the desirable transient power performances,  $P_H$  denotes the high-frequency component of power demand, and subscript  $H$ , which has the same meaning as that in  $ES_H$ , implies that the corresponding power should be balanced by the  $ES_H$ .

### C. Transient Power Allocation Among ESs

Combining (5) and (6), it is reasonable to infer that if the localized power converters are regulated by the ID controller, the power profiles of the converter will certainly resemble the current profiles as displayed in Fig. 4. Hence, the ID is highly suitable for the HESS consisting of ESs with high power density but limited energy density. It should be mentioned that the ID only compensates the transient power, and the coordination with the traditional linear  $V$ - $P$  droop, as described by (7), is needed to conveniently implement the energy management for HESS

$$V = V_n - m \times P_L \quad (7)$$

where  $P_L$  denotes the slow change of power demand and  $m$  is the droop coefficient determined by the ratio of the maximum allowed dc bus voltage deviation  $\Delta V_{\max}$  and the nominal power rating  $P_{\text{rating}}$  of a given  $ES_L$ , computed as

$$m = \frac{\Delta V_{\max}}{P_{\text{rating}}}. \quad (8)$$

It should be noted that the ID is assigned to the  $ES_H$  and the  $V$ - $P$  droop is used to regulate the output voltage of converters integrated with  $ES_L$ . Hence, the sum of  $P_H$  and  $P_L$  equals the lumped power demand  $P_d$ , given as

$$P_H + P_L = P_d. \quad (9)$$

By virtue of (6), (7) and (9), expressing  $P_H$  and  $P_L$  in terms of  $P_d$  gives the following equations:

$$P_H = \frac{s}{s + n/m} P_d \quad (10)$$

$$P_L = \frac{n/m}{s + n/m} P_d \quad (11)$$

where  $s$  is the Laplace operator. As can be seen from (10) and (11), the coordination of ID and  $V$ - $P$  intrinsically formulates the HPF and LPF in the HESS without any additional power allocation measures. The power demand is spontaneously decomposed into high-/low-frequency components and transient power allocation among ESs is consequently achieved. The ratio of droop coefficients ( $n/m$ ) is the cutoff angular frequency of HPF/LPF; it can be designed to satisfy the specified transient power allocation requirements. A smaller  $n/m$  drives the  $ES_H$  to compensate more transient power demand, which hence mitigates the stress of  $ES_L$ .

It is worth noting that (10) and (11) only reveal the power dynamics of the simplest system comprising an  $ES_H$  and an  $ES_L$ . However, when considering multiple  $ES_H$ s with different power capacities, the transient power sharing among  $ES_H$ s should also be carefully explored. Assuming there are total  $j$   $ES_H$  modules in the HESS, each of them is regulated by (6), which can be written in the  $s$  domain as follows:

$$V_i = V_n - \frac{n_i}{s} P_{Hi} \quad (12)$$

where  $i \in [1, j]$ . It is easy to show that  $P_{Hi}$  is inversely proportional to  $n_i$ , as described in the following equation:

$$P_{H1} : P_{H2} : \dots : P_{Hj} = \frac{1}{n_1} : \frac{1}{n_2} : \dots : \frac{1}{n_j}. \quad (13)$$

In this way, the transient power sharing among multiple different  $ES_H$ s can be conveniently achieved by appropriately tuning their respective ID coefficients, which is identical to the power sharing in the conventional  $V$ - $P$  droops. Combining (12) and (13), the equivalent ID equation is obtained as

$$V = V_n - \frac{n_{\text{eq}}}{s} P_H \quad (14)$$

where  $n_{\text{eq}} = (\sum_{i=1}^j \frac{1}{n_i})^{-1}$  and  $P_H = \sum_{i=1}^j P_{Hi}$ .

Observing (14), the multiple  $ES_H$ s can be simplified to an equivalent one, and the analysis from (9) to (11) also applies to the coordinated operation between  $ES_L$  and the equivalent  $ES_H$ . A scenario that transient power is shared by two  $ES_H$ s will be further discussed in Section V. For easy interpretation, the subsequent context regarding parameters design and system analysis will focus on the case only including one  $ES_H$  and one  $ES_L$ . It should be mentioned that the underlying assumption of deviation of (13) is that the HESS is integrated near the dc bus; the line impedance between converter output and dc bus can be neglected. However, if the line impedance is intolerable, the revised droop reported in [22] can be employed to compensate the voltage drop, and the analyses presented above still hold. To obtain better power management and even long-term economic operation, the decentralized control in this paper is also open to



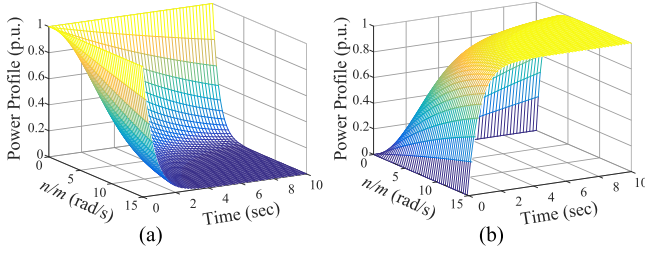


Fig. 5. Step responses of  $P_H$  and  $P_L$  with respect to the variation of  $n/m$ . (a)  $P_H$  profile. (b)  $P_L$  profile.

work with higher level controllers, such hierarchical control [5] and distributed control [17].

#### D. ID Coefficient Design

To better understand the power allocation, the expressions of  $P_H$  and  $P_L$  in the time domain can be obtained by evaluating the step response of (10) and (11), which are given as follows:

$$P_H = P_d e^{-\frac{n}{m}t} \quad (15)$$

$$P_L = P_d (1 - e^{-\frac{n}{m}t}). \quad (16)$$

The cutoff angular frequency  $n/m$  is a constant denoting the decay rate of the exponential term. The power dynamics of  $ES_H$  and  $ES_L$  are mainly determined by the value of  $n/m$ .  $P_H$  and  $P_L$  with respect to the variation of  $n/m$  are also displayed in Fig. 5.

Different from the  $V-P$  droop coefficient  $m$ , the ID coefficient  $n$  can be designed according to the ramp rate of  $ES_L$ . Following three assumptions are made:

1) the response time of  $ES_H$  is far smaller than that of  $ES_L$ , which means that the ramp rate of  $ES_H$  could be viewed to be infinite when compared to  $ES_L$ ;

2) the bandwidth of converter controllers is high enough to track the voltage references generated by ID/ $V-P$  controllers;

3) the power demand  $P_d$  in MG subjects to

$$P_d^* = \sup_{t \geq 0} |P_d(t)| \quad (17)$$

where  $\sup |\cdot|$  is the supremum of  $P_d$  along with time and  $P_d^*$  is the positive constant. Equation (17) implies that  $P_d$  is a finite value for all operational conditions, which is feasible in real cases.

Taking the derivative of (16), the power changing rate for a given  $n/m$  can be calculated as

$$\frac{dP_L}{dt} = P_d \cdot \frac{n}{m} \cdot e^{-\frac{n}{m}t}. \quad (18)$$

To ensure the safe operation of the HESS, the value of (18) should be less than or equal to the ramp rate  $r_{\text{ramp}}$  of  $ES_L$ . As  $P_d^*$  is defined as the maximum possible power demand, the worst case that the HESS feeds a load of  $P_d^*$  should also be taken into account when designing the ID coefficient  $n$ . The calculation of  $n$  can be found in the following equations:

$$\max \left( \frac{dP_L}{dt} \right) = P_d \cdot \frac{n}{m} \leq P_d^* \cdot \frac{n}{m} \leq r_{\text{ramp}} \quad (19)$$

$$n \leq \frac{r_{\text{ramp}} \cdot m}{P_d^*}. \quad (20)$$

#### E. Discussions

First, from a holistic perspective, power allocation problem has three different parts, power allocation among  $ES_H$ s, power allocation among  $ES_L$ s, and power allocation between  $ES_H$ s group and  $ES_L$ s group. For  $ES_H$ s, the high frequency  $P_d$  is allocated to each member of  $ES_H$ s according to their respective power capacity. For  $ES_H$ s, conventional  $V-P$  droop schemes are utilized to ensure the power shared by each  $ES_L$  is inversely proportional to their droop coefficients. Moreover, it is worth noting that multiple  $V-P$  droop controllers can be merged into an equivalent one, which is similar to (14). By virtual of the amalgamated ID and  $V-P$  droops, power allocation analysis detailed in (10) and (11) still holds.

Second, it should be mentioned that the proposed ID controller and  $V-P$  droop are interdependent. On the one hand, as an  $ES_H$  regulated by ID only provides high frequency power, it must coordinate with  $ES_L$  under  $V-P$  droop, which would handle the low frequency power. On the other hand, the existence of ID allows  $ES_L$  to refrain from providing/absorbing burst power, thus alleviating the stress of  $ES_L$  and considerably prolonging its lifespan. Hence, they have close pertinence to each other.

Third, to obtain the desirable performances of HESS,  $V-P$  droop coefficient and ID coefficient can be determined by (8) and (20), respectively. The design procedures are generalized methods that theoretically maintain free from the constraints such as converter volume, ES quantity, etc. The possible limitation is that the inner control loop response of the converter is overlooked. To avoid this concern, the PI design guidelines presented in the next section should be adopted to ensure the converter stability and desirable responding capability. Considering the scenario that numerous  $ES_L$ s and  $ES_H$ s simultaneously exist, they are fully controllable as all of them have their own interfacing converters. Then, multiple ID controllers and  $V-P$  droop controllers can be consolidated into equivalent ones. The transient power allocation scheme can be analyzed by (10) and (11), and the design of  $n_{\text{eq}}$  in (14) is also subjected to (20).

### III. OUTPUT IMPEDANCE SHAPING OF HESS BY ID

In Section II, it has been shown that the most attractive advantage of the ID controller is that, by correctly tuning the coefficient  $n$ , the output power changing rate of the interfacing converter can be flexibly designed to be less than the ramp rate of  $ES_L$ , which lengthen the lifetime of  $ES_L$ . It should be also noted that the ID not only helps to achieve these desirable transient performances, it can also stabilize the system feeding CPL by shaping the output impedance of the HESS.

#### A. PI Controller Design for Localized Converters

The realizations of both ID and  $V-P$  controllers are to generate respective voltage references for localized dc/dc bidirectional power converters. Only with the stable localized converter system, the power decomposition mechanism presented in Section II can be effectively achieved. Besides, the response speed of  $ES_L$  converter inner control loops should be adequately slow to mitigate the stress of  $ES_L$ , whereas the  $ES_H$  converter

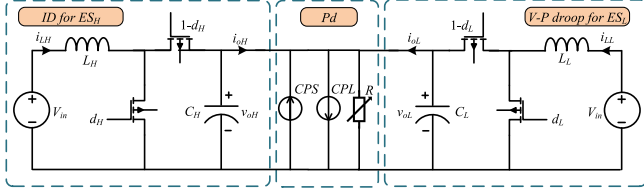


Fig. 6. Layout of parallel-connected bidirectional dc/dc converters for ID and V-P droop.

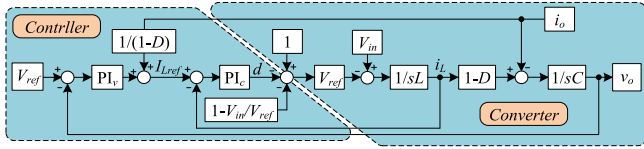


Fig. 7. Double PI controllers diagram for the localized dc/dc converter.

controller has to be sufficiently fast so that the burst power can be released by  $ES_H$  in the case of sudden load increase. The layout of the two boost converters connected in parallel is shown in Fig. 6, where the parameters accompanied by subscripts “H” and “L” correspond to the  $ES_H$  and  $ES_L$  respectively.  $i_{LH}$  and  $i_{LL}$  denote the inductor current of converters and are operated in continuous current mode.  $i_{oH}$  and  $i_{oL}$  are the output current of the two converters delivered to the loads.  $V_{oH}$  and  $V_{oL}$  are the terminal voltages that represent the dynamics of the output capacitors.  $d_H$  and  $d_L$  are the averaged duty cycle in a switching period. Dual-loop PI control is adopted for both converters to track the voltage references  $V_{ref}$  produced by ID and V-P, and the control diagram is presented in Fig. 7.  $PI_c$  and  $PI_v$  are the compensators of the current and voltage regulation loops, respectively, given as follows:

$$PI_c = \frac{k_{pc}s + k_{ic}}{s}, \quad PI_v = \frac{k_{pv}s + k_{iv}}{s} \quad (21)$$

where  $k_{pc}$ ,  $k_{ic}$ ,  $k_{pv}$ , and  $k_{iv}$  are the constants to be tuned. The  $V_{in}$  is the input voltage of ESs. The average duty cycle  $D$  is calculated by

$$D = 1 - \frac{V_{in}}{V_{ref}}. \quad (22)$$

As shown in Fig. 7, the complete control diagram consists of two segments: controller and converter. System disturbances, including constant value 1,  $V_{in}$  and  $i_o$ , are shown in the forward path of the converter. These disturbances can be counteracted by the feedforward terms in the controller so that PI compensators can function more precisely.

The main considerations of the compensators design can be concisely described as follows:

- 1) the response speed of current regulation should be slower than that of the PWM modulator and much faster than that of the voltage loop;
- 2) sufficient robustness of control loops should be guaranteed so that, in the case of large disturbances, the dominant poles of the system would not pass through imaginary axis and enter the right half complex plane;

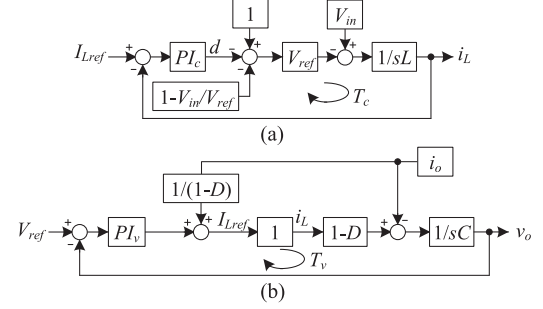


Fig. 8. Simplified current and voltage regulation loops. (a) Current regulation loop. (b) Voltage regulation loop.

- 3) the PI parameters should be flexibly tuned according to versatile requirements of pole positions in practice. Based on the above presumptions, the current and voltage regulation loops are individually illustrated in Fig. 8. When designing the voltage controller, the current loop is approximated as a unity gain due to its much faster response. In the following context, the PI compensators are designed by using pole placement method. The parameters with subscripts “c” and “v” are associated with the current and voltage regulation loops, respectively.

The closed-loop transfer function of the current control diagram, as shown in Fig. 8(a), is given as follows:

$$G_c = \frac{T_c}{1 + T_c} = \frac{(k_{pc}V_{ref}/L)s + (k_{ic}V_{ref}/L)}{s^2 + (k_{pc}V_{ref}/L)s + (k_{ic}V_{ref}/L)} \quad (23)$$

which exhibits a typical second-order system formed with two poles and one zero. The main idea of pole placement is to compute proper  $k_{pc}$  and  $k_{ic}$  such that the characteristic polynomial has the expected roots  $-\sigma_c \pm j\omega_c$ . Then, the desired polynomial is given as

$$[s - (-\sigma_c + j\omega_c)][s - (-\sigma_c - j\omega_c)] = s^2 + 2\sigma_c s + \omega_{nc}^2 \quad (24)$$

where  $\omega_{nc}^2 = \sigma_c^2 + \omega_c^2$ . Through matching the coefficients of (24) and denominator of (23), the PI parameters for current regulation loop are easily determined by

$$\begin{cases} \frac{k_{pc}V_{ref}}{L} = 2\sigma_c \\ \frac{k_{ic}V_{ref}}{L} = \omega_{nc}^2 \end{cases} \Rightarrow \begin{cases} k_{pc} = \frac{2\sigma_c L}{V_{ref}} \\ k_{ic} = \frac{\omega_{nc}^2 L}{V_{ref}} \end{cases}. \quad (25)$$

Substituting (25) into (23), the step response of (23) in time domain can be written as

$$G_c(t) = 1 + \frac{\omega_{nc}}{\omega_c} e^{-\sigma_c t} \sin(\omega_c t - \beta_c) \quad (26)$$

where  $\beta_c = \cos^{-1}(\sigma_c/\omega_{nc})$  is the lagging angle that belongs to  $(0, \pi/2)$ . The peak time  $t_{pc}$  can be computed by setting the first-order derivative of (26) to 0, given by the following equation:

$$G_c^{(1)}(t) \Big|_{t=t_{pc}} = 0 \Rightarrow t_{pc} = \frac{2\beta_c}{\omega_c}. \quad (27)$$

Furthermore, substituting (27) into (26) yields the peak value of (26), and the percent overshoot (P.O.<sub>c</sub>) of the step response of

the second-order system can be found in the following equation:

$$\text{P.O.}_c = (G_c(t_{pc}) - 1) \cdot 100\% = e^{-\frac{2\beta_c}{\tan(\beta_c)}} \cdot 100\%. \quad (28)$$

As observed from (28), the  $\text{P.O.}_c$  is only related to the ratio of  $\sigma_c$  and  $\omega_{nc}$ , and its minimum value can be found as  $e^{-2} \cdot 100\%$  (13.53%) by computing the limit of  $\text{P.O.}_c$  as  $\beta_c$  approaches zero. It is inferred that  $\beta_c$  is the stability indicator of the system (23), and a smaller  $\beta_c$  allows larger stability margin. In this section, the  $\text{P.O.}_c$  is restrained under 15% to ensure the stable system operation. The  $\beta_c$  can be consequently determined by

$$13.53\% < \text{P.O.}_c \leq 15\% \Rightarrow 0 < \beta_c \leq 0.1\pi. \quad (29)$$

Taking into account the worst case,  $\beta_c$  is set as  $0.1\pi$ , and referring to (26), the relation of  $\sigma_c$  and  $\omega_c$  is computed by

$$\omega_c = \sigma_c \tan(\beta_c). \quad (30)$$

In addition to the stability issues dominated by  $\beta_c$ , the response speed matching of control loops is another important problem. The settling time  $t_{sc}$  is usually defined as the time elapsed from the exertion of a step input to the time when the system output has entered and remained within a specified error band. In this sense,  $t_{sc}$  can be viewed as the indicator of response speed of (23), which can be computed by

$$\begin{aligned} \left| \frac{\omega_{nc}}{\omega_c} e^{-\sigma_c t} \right|_{t=t_{sc}} &= \left| \frac{e^{-\sigma_c t}}{\sin \beta_c} \right|_{t=t_{sc}} = \Delta_c, \quad 0 < \Delta_c \leq 5\% \\ \Rightarrow t_{sc} &= \frac{\ln(\sin \beta_c \cdot \Delta_c)^{-1}}{\sigma_c}. \end{aligned} \quad (31)$$

It is observed from (31) that once  $\beta_c$  is determined, a larger  $\sigma_c$  leads to shortened response time. Since the output signal of the current control loop is transferred to the modulator for PWM generation,  $t_{sc}$  should be at least ten times longer than the switching period  $T_{sw}$  of the carrier signal. Hence, the real part of the desired roots  $\sigma_c$  can be evaluated by

$$\sigma_c = \frac{\ln(\sin \beta_c \cdot \Delta_c)^{-1}}{k_c T_{sw}} \quad (32)$$

where  $k_c \geq 10$  is constant. Combining (28) and (31), it can be concluded that the stability margin of (23) is mainly dominated by the angle  $\beta_c$ , and the response time is determined by both  $\beta_c$  and  $\sigma_c$ . To meet the different requirements of system stability and response time in practices, the expected poles can be easily calculated by (30) and (32). Then,  $k_{pc}$  and  $k_{ic}$  are further identified by (25).

For the voltage regulation diagram shown in Fig. 8(b), the closed-loop transfer function is written by

$$G_v = \frac{T_v}{1 + T_v} = \frac{(k_{pv}(1-D)/C)s + k_{iv}(1-D)/C}{s^2 + (k_{pv}(1-D)/C)s + k_{iv}(1-D)/C}. \quad (33)$$

Similar to (30) and (32), the imaginary and real parts of the designated poles for (33) can be given as the follows:

$$\omega_v = \sigma_v \tan(\beta_v) \quad (34)$$

$$\sigma_v = \frac{\ln(\sin \beta_v \Delta_v)^{-1}}{k_v k_c T_{sw}} \quad (35)$$

where  $\beta_v = \beta_c = 0.1\pi$  is the measurement of  $\text{P.O.}_v$ ,  $\Delta_v = \Delta_c = 5\%$  is the percent error band for determining the settling time, And  $k_v \geq 10$  is a positive constant, which means that the response time of the voltage regulation loop is at least ten times longer than that of the current loop. The corresponding  $k_{pv}$  and  $k_{iv}$  in (33) can also be evaluated by

$$\begin{cases} \frac{k_{pc}(1-D)}{C} = 2\sigma_v \\ \frac{k_{ic}(1-D)}{C} = \omega_{nv}^2 \end{cases} \Rightarrow \begin{cases} k_{pv} = \frac{2\sigma_v C}{1-D} \\ k_{iv} = \frac{\omega_{nv}^2 C}{1-D} \end{cases} \quad (36)$$

where  $\omega_{nv}^2 = \sigma_v^2 + \omega_v^2$ .

The salient advantage of the compensator design using pole placement over those design approaches using bode plot is that the PI parameters are directly and intuitively related to the required response time and the allowed maximum overshoot of system step response in time domain. This is highly useful for HESS because the controllers of converters should strictly work in coordination. Especially for that  $\text{ES}_H$ , the settling time of voltage and current regulation loops should be smaller enough in order to release sufficient power to load in system transition.

### B. Minimum Relative Impedance Criterion

As discussed earlier, the presence of CPLs, unfortunately, poses threats to the stable operation of the entire MG. To examine the stability of the studied system, a conventional way is to establish state-space equations of the complete system based on a small signal model by linearizing the plant around an equilibrium operating point. However, it is worth mentioning that MGs are complicated by numerous energy sources and energy conversion devices. The RESs and distributed loads are highly intermittent and uncertain. Therefore, it is very difficult to obtain a fixed MG model and further use it to access the stability of the system.

Impedance matching method provides an elegant way to explore the stability of MG containing multiple cascaded devices [23], [24]. The central idea of this method is to establish an equivalent Thevenin model comprising the voltage source and the output impedance. The ratio of the source output impedance and load input impedance is regarded as the generalized minor loop (GML) of the cascaded system [23]. On this basis, several stability criteria have been reported, such as Middlebrook criterion, gain margin phase margin criterion, passivity-based stability criterion, etc [24]. Yet these criteria are normally criticized for conservativeness and they ultimately originate from Nyquist criterion. In fact, for a closed-loop control system, system stability can be ensured as long as the minor loop abides by Nyquist criterion, and this principle also applies to the HESS studied in this paper. If Nyquist contour of GML does not anticlockwise encircle the critical point  $(-1, j0)$ , then the cascaded system is stable. The equivalent circuit corresponding to the layout shown in Fig. 6 is illustrated in Fig. 9.  $V_{eqH}$  and  $V_{eqL}$  are the equivalent voltage sources.  $Z_H$  and  $Z_L$  denote the output impedances and  $Z_{load}$  represents the linearized lumped impedance of  $P_d$ . It has been proved that CPS and resistive load help to stabilize the dc bus [20]. To examine the system stability under the worst case,

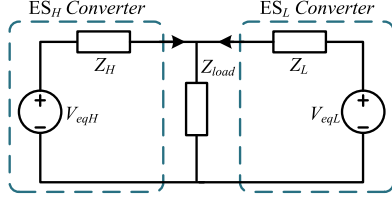


Fig. 9. Equivalent Thevenin circuit of the cascaded system consisting of  $ES_L$ ,  $ES_H$ , and load.

CPL is considered in this section as the only power consumer. Therefore, the power of CPL should be equal to  $P_d$  and the impedance of CPL can be computed in the following equation:

$$Z_{load} = Z_{CPL} = -\frac{V_b^2}{P_d} \quad (37)$$

where  $V_b$  is the dc bus voltage.

It should be noted that the boost converters are inherently the nonlinear systems that contain bilinear terms coupling the control input and state variables together [25]. To derive the equivalent output impedance of converters integrated with  $ES_H$  and  $ES_L$ , the small signal model is established by linearizing the individual converter system. The linearized state-space equations of the  $ES_H$  and  $ES_L$  subsystems are given as follows:

$$\Delta \dot{\mathbf{X}}_H = \mathbf{A}_H \Delta \mathbf{X}_H + \mathbf{B}_H \Delta i_{oH} \quad (38)$$

$$\Delta \dot{\mathbf{X}}_L = \mathbf{A}_L \Delta \mathbf{X}_L + \mathbf{B}_L \Delta i_{oL} \quad (39)$$

where  $\mathbf{A}_H$  and  $\mathbf{A}_L$  are the state matrices, and  $\mathbf{B}_H$  and  $\mathbf{B}_L$  are the input matrices. The detailed derivations of (38) and (39) are provided in the appendix. The  $\Delta \mathbf{X}_H$  and  $\Delta \mathbf{X}_L$  represent the state vectors, which are expressed by the following equations:

$$\Delta \mathbf{X}_H = [\Delta v_{oH} \ \Delta i_{LH} \ \Delta \xi_{1H} \ \Delta \xi_{2H} \ \Delta \xi_{3H}]^T \quad (40)$$

$$\Delta \mathbf{X}_L = [\Delta v_{oL} \ \Delta i_{LL} \ \Delta \xi_{1L} \ \Delta \xi_{2L}]^T. \quad (41)$$

In (40),  $\Delta \xi_{1H}$ ,  $\Delta \xi_{2H}$ , and  $\Delta \xi_{3H}$  denote the state variables in ID, voltage PI controller, and current PI controller of  $ES_H$  subsystem. Similarly, in (41),  $\Delta \xi_{1L}$  and  $\Delta \xi_{2L}$  are the state variables in voltage and current PI controllers of  $ES_L$  subsystem. Based on (38) and (39), the output impedances of the two subsystems are given as follows:

$$Z_H = -\frac{\Delta v_{oH}}{\Delta i_{oH}} = \mathbf{C}_H (s\mathbf{I} - \mathbf{A}_H)^{-1} \mathbf{B}_H \quad (42)$$

$$Z_L = -\frac{\Delta v_{oL}}{\Delta i_{oL}} = \mathbf{C}_L (s\mathbf{I} - \mathbf{A}_L)^{-1} \mathbf{B}_L \quad (43)$$

where  $\mathbf{C}_H = [-1 \ 0 \ 0 \ 0]$  and  $\mathbf{C}_L = [-1 \ 0 \ 0]$  are the constant matrices. The total output impedance  $Z_{HL}$  of HESS is the equivalent impedance of the parallel-connected  $Z_H$  and  $Z_L$ , which is computed by

$$Z_{HL} = Z_H // Z_L = \frac{Z_H Z_L}{Z_H + Z_L}. \quad (44)$$

Combining (37) and (44) yields the GML of the cascaded system, given as follows:

$$\text{GML} = \frac{Z_{HL}}{Z_{CPL}}. \quad (45)$$

TABLE I  
SYSTEM PARAMETERS

Parameter	Description	Value
$V_n$	Nominal voltage reference	170 V
$\Delta V_{max}$	Maximum allowed voltage deviation	$\pm 10$ V
$L_H, L_L$	Converter inductors	2 mH
$C_H, C_L$	Converter capacitors	470 $\mu$ F
$\beta_v, \beta_c$	Phase lag in (27) and (31)	$0.1\pi$
$\Delta_v, \Delta_c$	Specified error band	5%
$f_{sw}$	Switching frequency	20 kHz

TABLE II  
PARAMETERS FOR HESS<sub>I</sub> AND HESS<sub>II</sub>

HESS Type	CPL (kW)	V-P droop coefficient $m$	ID droop coefficient $n$
I	2/3/4	$m_I = 0.01$	$0.01 \cdot 2\pi$
II		$m_{II} = 0.02$	Null

The stability of HESS can be then studied by investigating if GML adheres to the Nyquist criterion. It is easy to know from (37) that  $Z_{CPL}$  is a negative constant when the CPL power and bus voltage are given. Therefore, a MRIC, which is a new extension of Nyquist criterion, is specially derived for a cluster of systems integrated with CPLs, in order to realize convenient stability analysis, as presented by the following equation:

$$\begin{aligned} \text{real} \left( \frac{Z_{HL}}{Z_{CPL}} \right) &> -1 \\ \Rightarrow \text{real}(-Z_{HL}) - Z_{CPL} &> 0 \\ \Rightarrow \min[\text{real}(-Z_{HL})] - Z_{CPL} &> 0 \end{aligned} \quad (46)$$

where  $\text{real}(\cdot)$  denotes the real part of a complex value. Accordingly, the MRIC stability margin  $\gamma_{ZHL}$  of HESS feeding CPL is defined as

$$\gamma_{ZHL} = \min[\text{real}(-Z_{HL})] - Z_{CPL}. \quad (47)$$

$\gamma_{ZHL}$  actually measures how far the  $-Z_{HL}$  Nyquist contour is from that of  $Z_{CPL}$ , which also equivalently indicates the gain margin in the  $Z_{HL}/Z_{CPL}$  Nyquist plot. Hence,  $(Z_{CPL}, j0)$  serves as the critical point under MRIC as  $(-1, j0)$  does in the conventional Nyquist criterion.

### C. HESS Output Impedance Shaping by ID

The converter parameters in Fig. 6 and the controllers in Fig. 7 are provided in Table I. To expound the impedance shaping and stabilization effect of the proposed ID controller, two different types of HESS with the same total V-P droop characteristics are adopted in this part. The HESS consisting of  $ES_L$  ( $m_I = 0.01$ ) and  $ES_H$  ( $n = 0.01 \cdot 2\pi$ ) is referred to as type I, denoted as HESS<sub>I</sub>, whereas another type of HESS, expressed as HESS<sub>II</sub>, is assumed to have two  $ES_L$ s whose interfacing converters are connected in parallel with V-P droop coefficients twice of  $m_I$  ( $m_{II} = 0.02$ ). The parameters of these two comparative HESS types are listed in Table II. For HESS<sub>I</sub>, the steady dc bus voltage is dominated by  $ES_L$  because  $ES_H$  only compensates



TABLE III  
PARAMETERS FOR STABILITY TESTING

CPL (kW)	V-P droop coefficient $m$	ID droop coefficient $n$
4	0.01	$n_1 = 0.01 \cdot 1\pi$ $n_2 = 0.01 \cdot 2\pi$ $n_3 = 0.01 \cdot 3\pi$

high frequency transient power. Whereas for HESS<sub>II</sub>, the equivalent droop coefficient  $m_{eq}$  of the whole HESS<sub>II</sub> can be calculated as  $m_{eq} = m_{II}/2$ , which equals  $m_I$  [5]. Therefore, given that HESS<sub>I</sub> and HESS<sub>II</sub> are loaded by the same CPL, the bus voltage of the two system are also identical in the steady state.

Following the reasoning in Section III-B, the output impedance of HESS<sub>I</sub> is signified by  $Z_{HL}$  as in (44), and accordingly the output impedance  $Z_{LL}$  of HESS<sub>II</sub> can be also written as

$$Z_{LL} = \frac{Z_L}{2} \Big|_{m_{II}=0.02}. \quad (48)$$

By means of the definition of (47), the stability margin tests of HESS<sub>I</sub> and HESS<sub>II</sub> under three different load conditions (CPL = 2 kW/3 kW/4 kW) are shown in Fig. 10. The  $\gamma_{ZHL}/\gamma_{ZLL}$  represent the relative distance between the minimum real part of  $-Z_{HL}/-Z_{LL}$  and  $Z_{CPL}$ . It can be observed from Fig. 10(a) that when CPL is scheduled as 2 kW, the critical point is  $(-11.25, j0)$ . The  $\gamma_{ZHL}$  and  $\gamma_{ZLL}$  are estimated as 10.34 and 6.6, respectively, which reveals that HESS<sub>I</sub> is more stable than HESS<sub>II</sub>.

The similar results can also be found in Fig. 10(b), in which CPL increases to 3 kW, and the corresponding critical point moves to  $(-6.53, j0)$ . For this scenario,  $\gamma_{ZHL} = 3.23$  is still larger than  $\gamma_{ZLL} = 1.43$ , which verifies the effectiveness of output impedance shaping mechanism and stabilization functionality of the proposed ID controller. By comparing MRIC stability margin in the cases of 2- and 3-kW CPLs, it is obvious that the growth of CPL decreases the stability margin of both systems.

Fig. 10(c) shows an extreme situation, where CPL rises to 4 kW and the steady dc bus voltage drops to 130 V, which is rigorously not allowed in practice. Fortunately, it can be seen that, even in this atrocious condition, the stability margin  $\gamma_{ZHL}$  of HESS<sub>I</sub> still remains around 0.995. However, the Nyquist contour of  $-Z_{LL}$  of HESS<sub>II</sub> has encircled the critical point  $(-4.23, j0)$ , and system instability will be induced.

Another interesting finding is that, despite the changes of CPL, the minimum real part of  $-Z_{HL}$  almost maintains at about 3.32, and the stability margin changes are mainly caused by the motion of the critical point. This characteristic is greatly favored by the HESS designers to determine the maximum permitted load for ensuring system stable operations.

To further examine the impact of ID coefficient  $n$  on the impedance shaping, three different values of  $n$  implemented on HESS<sub>I</sub> are listed in Table III, where CPL 4 kW is considered. The comparative stability margin test is conducted in Fig. 11. It is recognized that the decrease of  $n$  tends to enlarge the stability margin. This is fairly comprehensible from the perspective

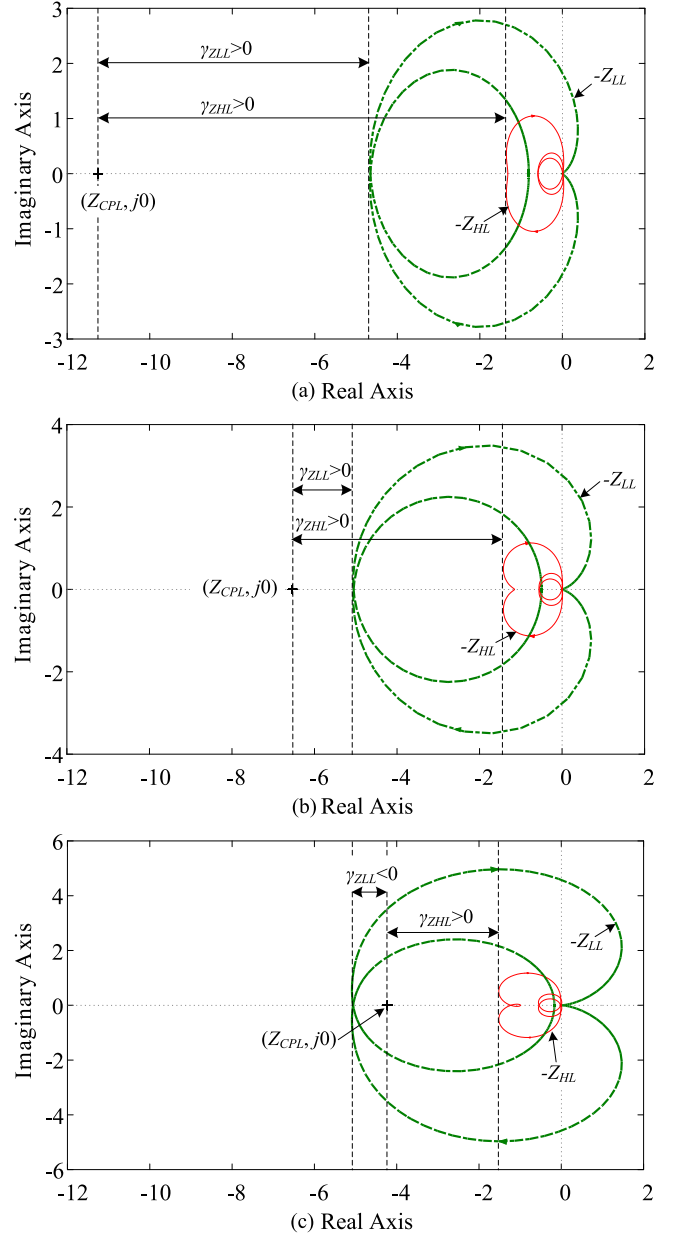


Fig. 10. Nyquist contour of  $-Z_{LL}$  and  $-Z_{HL}$  and stability margin comparisons with the increase of CPL: (a) CPL = 2 kW; (b) CPL = 3 kW; and (c) CPL = 4 kW.

of transient power allocation pattern that  $n/m$  acts as the cutoff angular frequency of HPF/LPF and a smaller  $n/m$  drives  $ES_H$  to compensate more high frequency power demand. By the analogy between (5) and (6),  $n$  can be viewed as the indicator of the capacitive effect that ID can provide for the dc bus. If a small value of  $n$  is assigned to ID, then  $ES_H$  is much stronger to smooth the dc bus voltage, and in this way, the bus can be stabilized.

#### IV. SIMULATIONS

To verify the effectiveness of the proposed ID controller, the HESS shown in Fig. 6 was modeled in MATLAB/Simulink environment, and simulation results are presented. System parameters are listed in Table I. It is known that, from the impedance

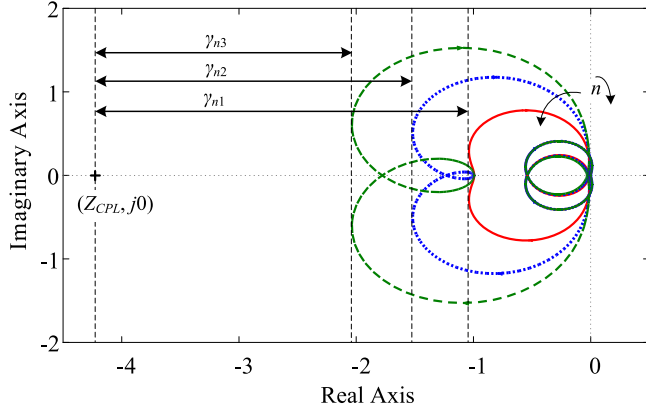


Fig. 11. Nyquist contour of  $-Z_{HL}$  and stability margin comparisons with the variation of ID droop coefficient:  $n_1 = 0.01 \cdot 1\pi$ ;  $n_2 = 0.01 \cdot 2\pi$ ; and  $n_3 = 0.01 \cdot 3\pi$ .

perspective, the existence of resistive loads and CPS would not jeopardize the overall system stability. The most intractable scenario is that the lumped load of HESS is only dominated by CPL. Hence, in this section, HESS loaded by CPL is considered, and neither resistive load nor CPS is involved. The subsequent context will investigate the power allocation performances under ID coefficient variation. It will also show that an improper PI controller design will unfavorably cause transient power oscillations in system transition. Additionally, the output impedance shaping for HESS by ID will be validated to stabilize the whole system through time-domain simulations of HESS<sub>I</sub> and HESS<sub>II</sub>.

#### A. Case 1

As mentioned earlier, the coordinated operation with ID and V-P droop naturally decompose the power demand into high-frequency and low-frequency ones, which are further allocated to ES<sub>H</sub> and ES<sub>L</sub>, respectively. The power dynamics of the HESS feeding 300-W CPL are visible in Fig. 12. When the load step-up and step-down are triggered at 0.5 and 8 s, the ES<sub>H</sub> immediately responds to compensate the load power of fast change and gradually decrease to zero in a short time, whereas the power of ES<sub>L</sub> smoothly rise from 0 to 300 W and consistently handle the whole load power in the steady state.

According to power dynamics depicted by (15) and (16), the ratio of  $n$  and  $m$  would remarkably affects the transient power allocation performances. The V-P coefficient  $m$ , which is in principle computed by (8), is assumed to be a constant 0.01 in this paper. Observing the different power profiles displayed in Fig. 12, the transient durations of the scenarios with  $n$  set as  $0.01 \cdot 1\pi$ ,  $0.01 \cdot 2\pi$ , and  $0.01 \cdot 3\pi$  are around 6, 4, and 2 s, respectively. The simulation results are in good agreement with the analysis in Section II-C. Therefore, it can be concluded that the lowered ID coefficient drives the ES<sub>H</sub> to compensate more transient power and the stress of ES<sub>L</sub> is mitigated.

#### B. Case 2

As discussed in Section III-A, the parameters  $\beta_c = \beta_v$  dominate the stability margin of (23) and (33), while  $\Delta_c = \Delta_v$  are mostly related to the response speed of the closed-loop systems.

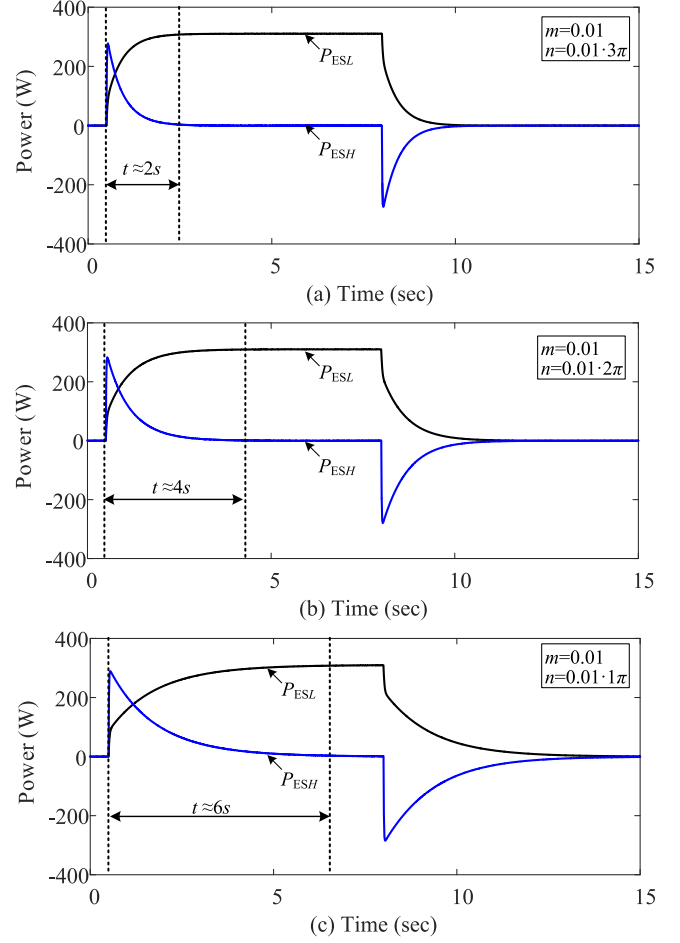


Fig. 12. Transient power allocation among ES<sub>H</sub> and ES<sub>L</sub>.

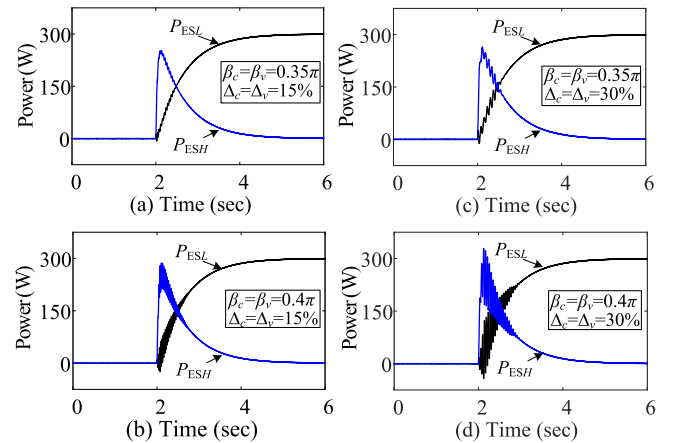


Fig. 13. Transient power oscillations caused by the improper design of PI controller.

The ideal ranges of these parameters design have been given in (29) and (31). In case 2,  $m$  and  $n$  are selected as 0.01 and  $0.01 \cdot 2\pi$ , respectively. The scenarios, in which the  $\beta_c$ ,  $\beta_v$ ,  $\Delta_c$ , and  $\Delta_v$  are chosen beyond the constraints of (29) and (31), are examined. Simulation results under different parameter settings are shown in Fig. 13. Comparing Fig. 13(a) and (b), when  $\Delta_c$  and  $\Delta_v$  are selected as 15%, more severe power oscillation is

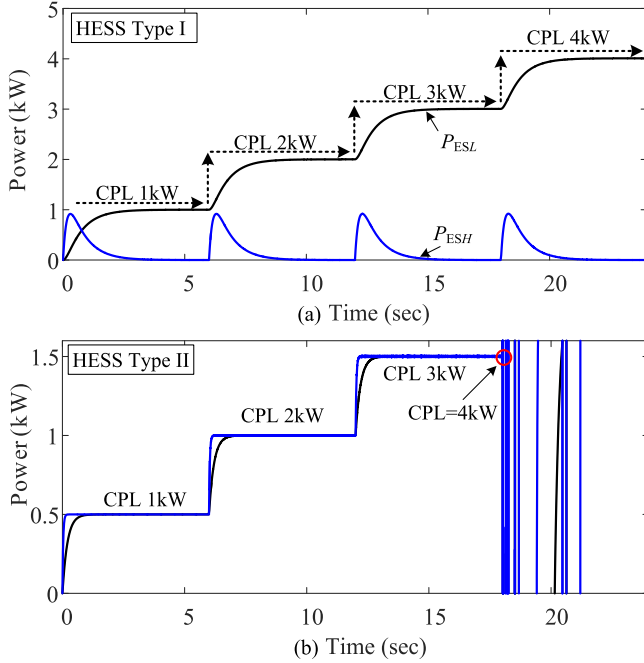


Fig. 14. Power profiles of HESS<sub>I</sub> and HESS<sub>II</sub> with consecutive CPL step-up.

observed in the case of  $\beta_c = \beta_v = 0.4\pi$ . The same result can also be found through the comparison of Fig. 13(c) and (d). The reason for these findings is that, as indicated by (28), the increased values of  $\beta_c$  and  $\beta_v$  may result in overlarge P.O. and hence the instability would be induced.

On the other hand, by scrutinizing Fig. 13(a) and (c), both  $\beta_c$  and  $\beta_v$  are assigned as  $0.35\pi$ , and power oscillation is less damped when  $\Delta_c$  and  $\Delta_v$  equal 30%. This fact is supported by the previous analysis in (31) that the rising  $\Delta_c$  and  $\Delta_v$  weaken the constraint on final value convergence of step response. Consequently, as suggested by (32) and (35), the absolute value of the designated pole real part would be lowered, which challenges the stability of the converter system. Fig. 13(d) gives the worst transient power performance that the four parameters go far beyond the predefined ranges, which is rigorously not permitted in real applications.

### C. Case 3

It has been proved in Sections III-B and III-C that the adoption of ID helps to shape the output impedance of HESS by keeping the minimum real part of  $-Z_{HL}$  far away from MRIC critical point. As a result, through the comparative studies of HESS<sub>I</sub> and HESS<sub>II</sub>, the ID allows augmented stability margin upon MRIC. The time-domain simulations of the two type of HESSs under consecutive step-up of CPL are demonstrated in Fig. 14. From Fig. 14 (a), the transient power allocation in HESS<sub>I</sub> continuously functions well and the system stability is also ensured even though the CPL rises to 4 kW. While proceeding to Fig. 14(b), the instability of HESS<sub>II</sub> unexceptionally occurs when CPL of 4 kW is exerted at 18 s. These results validate the stability analysis in Fig. 10(c) that the MRIC criterion is violated because the critical point is enclosed by the Nyquist contour of  $-Z_{LL}$ .

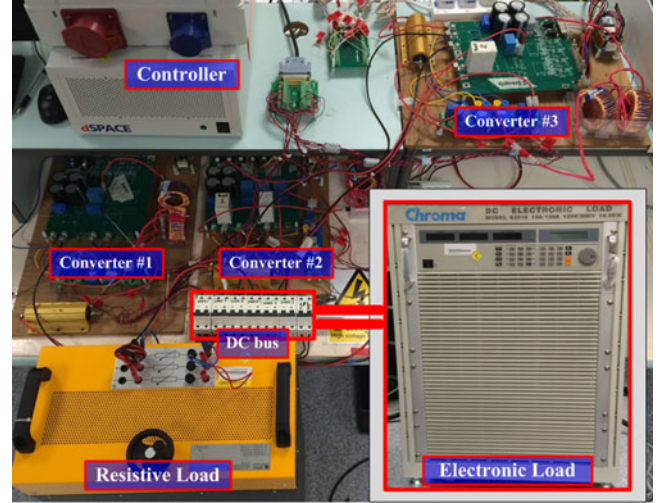


Fig. 15. Experimental setup.

TABLE IV  
CASES FOR EXPERIMENTAL VERIFICATION

	Converter #1	Converter #2	Converter #3
Case 4	V-P	ID	Idle
Case 5	V-P	ID	CPS
Case 6	V-P	ID	ID

## V. EXPERIMENTAL VERIFICATIONS

For experimental verifications, an in-house platform was established, as shown in Fig. 15. System parameters are the same as in the simulations and have been already listed in Table I. For convenience, both resistive load and CPL are incorporated in the dc system, which has three converters. The electronic load is always configured as the CPL. The operation modes of converters in the following three different cases are summarized in Table IV.

### A. Case 4

In this case, the HESS is assumed to operate under discharging mode, and converter #1 ( $ES_L$ ) is assigned with conventional V-P droop, whereas converter #2 ( $ES_H$ ) is regulated under ID control. Converter #3 is in idle mode and CPS is not involved. The transient power allocation between the  $ES_H$  and  $ES_L$  considering ID coefficient variations can be seen in Fig. 16. To start with, the HESS is operating in a steady state, and the  $ES_L$  continuously delivers power to the resistive load while the power of  $ES_H$  maintains at zero. When the CPL is enabled and disabled in sequence, it is clear that  $ES_H$  tends to compensate the demand load of high frequency and the  $ES_L$  responds to the load change much slower than  $ES_H$ . Meanwhile, the individual output voltage of both ESs slightly drops.

Another finding is that a larger ID coefficient gives rise to a faster response of the whole HESS, and the total power supplied by  $ES_H$  accordingly decreases to zero after system transition. The experimental results of this case are fully consistent with the

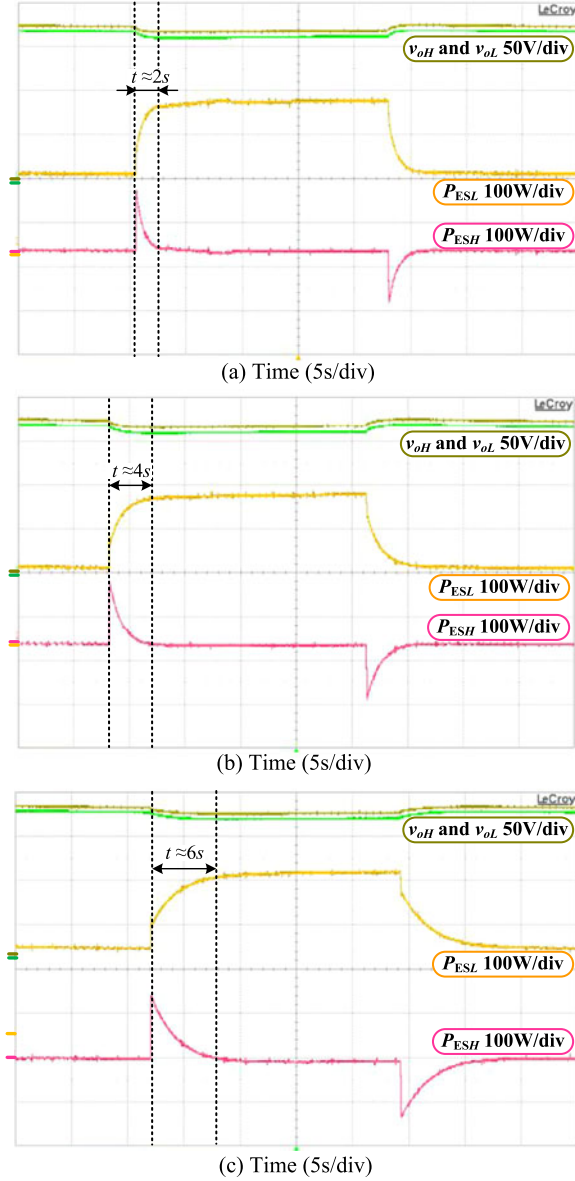


Fig. 16. Transient power allocation among ESs when HESS is discharged.

simulations as in case 1, which again validate the effectiveness of the proposed ID controller and relevant analysis in Section II-C.

### B. Case 5

Apart from the fact that the HESS release power when power deficiency is detected, on the other hand, in the case that the surplus power is induced, the HESS should also correctly function in the charging mode. Case 5 investigates the transient power performances of  $ES_H$  and  $ES_L$  when they are both charged. As indicated by Table IV, different from case 4, converter #3, in this case, is simulated as a CPS that directly injects 2-A current into the system regardless of dc bus deviation. As the resistive load is deliberately regulated to be light, CPS entirely compensates the resistive power and then the remaining CPS power has to be absorbed by HESS. The corresponding experimental results are illustrated in Fig. 17.

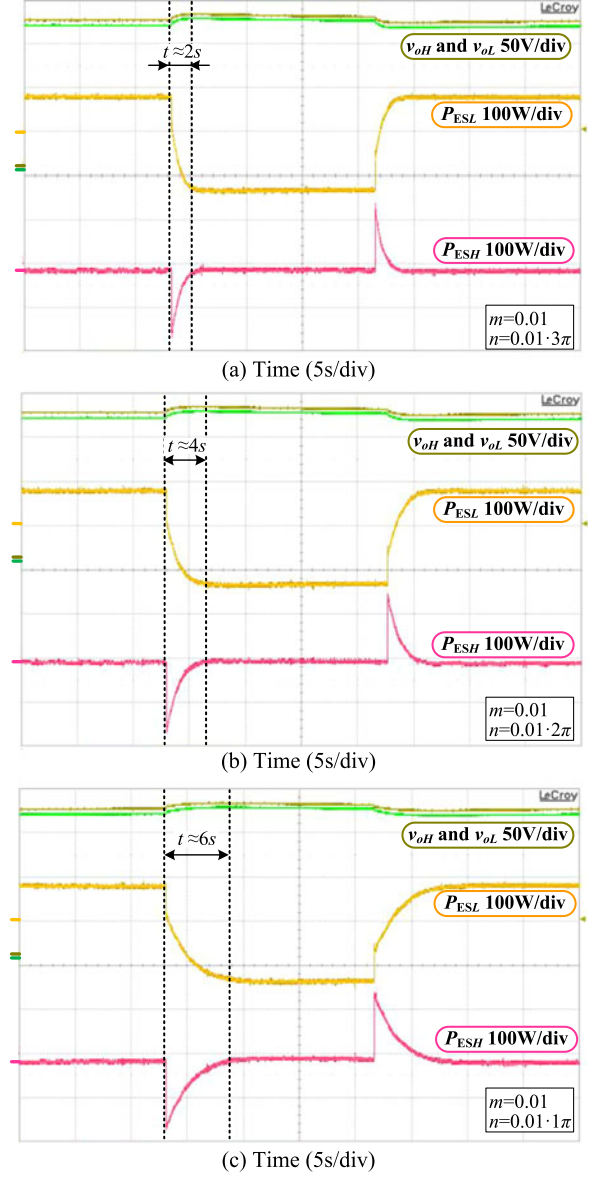


Fig. 17. Transient power allocation among ESs when HESS is charged.

It is visible that when converter #3 is activated,  $ES_H$  and  $ES_L$  concurrently absorb power from the dc bus, while the power allocation mechanism formulated by coordination of  $V$ - $P$  droop and ID still functions effectively. This means that the proposed ID controller retains the bidirectional power flow of HESS, which makes it flexible to realize the power management in HESS.

### C. Case 6

It is known that multiple converters connected in parallel are quite common in the MG system. The paralleled operations and the equivalent pattern of traditional  $V$ - $P$  droop controllers have been extensively studied in the literature [5], [26]. Hence, case 6 assumes that converter #1 is with the  $V$ - $P$  droop whereas converter #2 ( $ES_{H1}$ ) and converter #3 ( $ES_{H2}$ ) are under ID controllers with different droop coefficients ( $n_1$



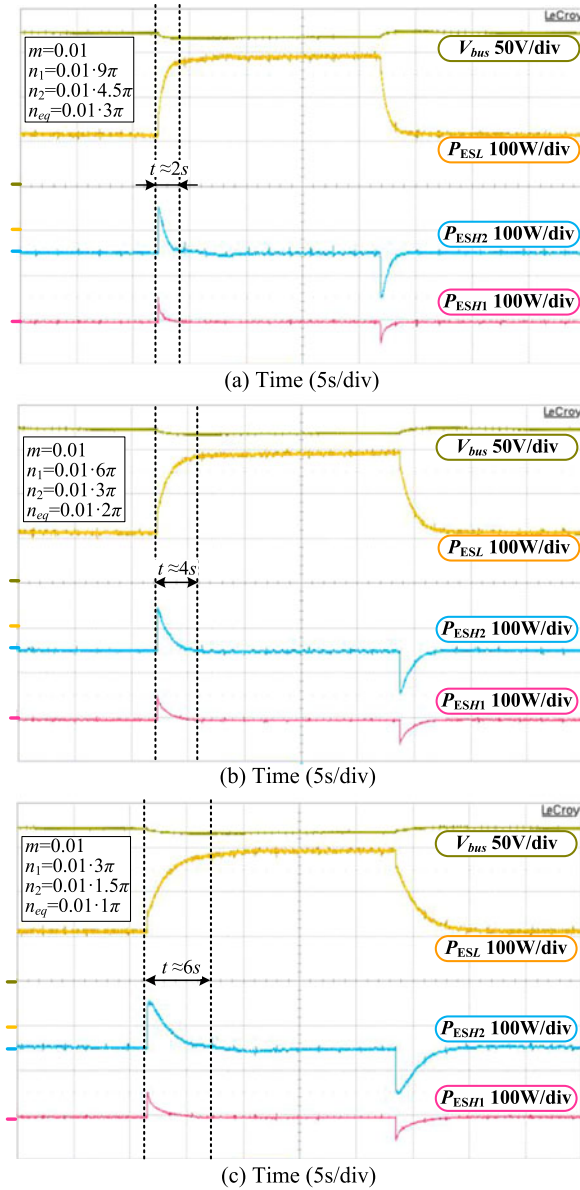


Fig. 18. Transient power allocation among one  $ES_L$  and two  $ES_H$ s.

and  $n_2$ ). This case focuses on the transient power sharing between two  $ES_H$ s. The HESS is also working in discharging mode and the CPL is neglected. The relevant experimental results are plotted in Fig. 18. It can be seen that the  $V$ - $P$  droop coefficient  $m$  and the overall equivalent ID coefficient  $n_{eq}$  in all three scenarios remain identical to those in the previous cases. As a result, when CPL step-up and step-down are exerted, the system transient durations keep invariant, which are 2, 4, and 6 s, respectively. Moreover, based on (10), (11), and (14), it is straightforward to recognize that the total power  $P_H$  and  $P_L$  supplied by  $ES_H$ s and  $ES_L$  also remain unchanged.

As detailed in Fig. 18, it is worth noting that the fast-changing power demand is simultaneously shared by  $ES_{H1}$  and  $ES_{H2}$  respectively. Despite the alteration of  $n_{eq}$ , on the condition that  $n_1$  is set two times of  $n_2$ , the corresponding power delivered by  $ES_{H1}$  is half of that by  $ES_{H2}$ , which is perfectly in line with

the analysis given in (13). This transient power sharing scheme among ID controllers elegantly allows for the convenient HESS extension and provides efficacious assistance for EMS design.

## VI. CONCLUSION

This paper proposes an ID for a class of ESs with fast response to obtain transient power allocation in HESS. By cooperation of ID and  $V$ - $P$  droop, the high-frequency components of power demand and the low frequency ones are, respectively, assigned to the  $ES_H$  and  $ES_L$ . The ID coefficient  $n$  is carefully designed according to the nominal ramp rate of  $ES_L$ , intending to prolong the lifespan of HESS. The practical PI controllers design method for dc/dc converters using pole placement is also provided. The prominent advantage of this method is directly relating the PI parameters to the controller response in the time domain, which facilitates the design of HESS. To further evaluate the stability of the whole system, the MRIC is derived based on Nyquist criterion especially for a class of systems feeding CPLs. According to MRIC, the proposed ID exhibits the stabilization effect on HESS by shaping the output impedance of the system. Simulations and experimental results have validated the feasibility and effectiveness of the ID. Proceeding to apply the proposed ID controller in the real systems, the power fluctuation of RESs can be modeled as the superposition of repeated power increase/decrease. The expected result is that the transient power allocation dynamics shown in the experiments would consecutively appear with time lapse. The overall control performances of HESS will not be impaired and the control accuracy can also be attained as in the experimental consequences.

## APPENDIX

Returning to Fig. 6, the dynamic average model of the converters for  $ES_H$  and  $ES_L$  is given as follows:

$$\begin{cases} C_H \frac{dv_{oH}}{dt} = (1 - d_H)i_{LH} - i_{oH} \\ L_H \frac{di_{LH}}{dt} = v_{in} - (1 - d_H)v_{oH} \end{cases} \quad (A1)$$

$$\begin{cases} C_L \frac{dv_{oL}}{dt} = (1 - d_L)i_{LL} - i_{oL} \\ L_L \frac{di_{LL}}{dt} = v_{in} - (1 - d_L)v_{oL} \end{cases} \quad (A2)$$

Performing the small signal disturbances on (A1) and (A2) yields the linearized model as follows:

$$\Delta \dot{\mathbf{x}}_{1H} = \mathbf{A}_{1H} \Delta \mathbf{x}_{1H} + \mathbf{B}_{1H} \Delta d_H + \mathbf{C}_{1H} \Delta i_{oH} \quad (A3)$$

$$\Delta \dot{\mathbf{x}}_{1L} = \mathbf{A}_{1L} \Delta \mathbf{x}_{1L} + \mathbf{B}_{1L} \Delta d_L + \mathbf{C}_{1L} \Delta i_{oL} \quad (A4)$$

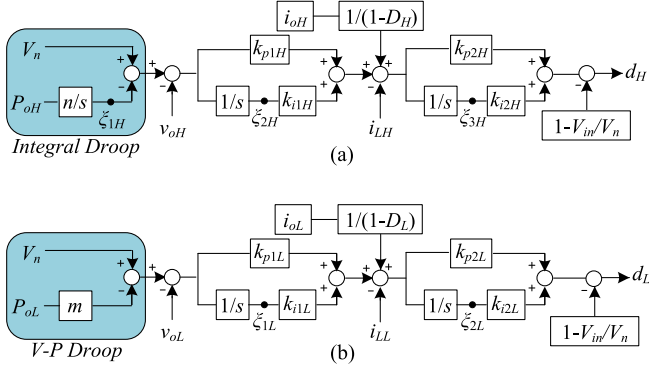


Fig. 19. Controllers for  $ES_H$  and  $ES_L$ . (a) Integral droop and double PI controllers. (b) V-P droop and double PI controllers.

where

$$\begin{aligned} \Delta \mathbf{x}_{1H} &= [\Delta v_{oH} \quad \Delta i_{LH}]^T, \quad \Delta \mathbf{x}_{1L} = [\Delta v_{oL} \quad \Delta i_{LL}]^T \\ \mathbf{A}_{1H} &= \begin{bmatrix} 0 & \frac{1-D_H}{C_H} \\ \frac{D_H-1}{L_H} & 0 \end{bmatrix}, \quad \mathbf{A}_{1L} = \begin{bmatrix} 0 & \frac{1-D_L}{C_L} \\ \frac{D_L-1}{L_L} & 0 \end{bmatrix} \\ \mathbf{B}_{1H} &= \begin{bmatrix} -\frac{I_{LH}}{C_H} & \frac{V_{CH}}{L_H} \end{bmatrix}^T, \quad \mathbf{B}_{1L} = \begin{bmatrix} -\frac{I_{LL}}{C_L} & \frac{V_{CL}}{L_L} \end{bmatrix}^T \\ \mathbf{C}_{1H} &= [-\frac{1}{C_H} \quad 0]^T, \quad \mathbf{C}_{1L} = [-\frac{1}{C_L} \quad 0]^T. \end{aligned}$$

To derive the full model of each converter, based on Fig. 7, the complete controllers for  $ES_H$  and  $ES_L$  are detailed in Fig. 19, where  $d_H$  and  $d_L$  are the control input of the converters. It is observed that  $\xi_{1H}$ ,  $\xi_{2H}$ ,  $\xi_{3H}$ ,  $\xi_{1L}$ , and  $\xi_{2L}$  are the state variables inside the controllers, and their dynamic models can be written as the following equations:

$$\begin{cases} \frac{d\xi_{1H}}{dt} = nP_{oH} = ni_{oH}v_{oH} \\ \frac{d\xi_{2H}}{dt} = V_n - \xi_{1H} - v_{oH} \\ \frac{d\xi_{3H}}{dt} = k_{p1H} \frac{d\xi_{2H}}{dt} + k_{i1H} \xi_{2H} + \frac{i_{oH}}{1-D_H} - i_{LH} \end{cases} \quad (A5)$$

$$\begin{cases} \frac{d\xi_{1L}}{dt} = V_n - mP_{oL} - v_{oL} = V_n - mi_{oL}v_{oL} - v_{oL} \\ \frac{d\xi_{2L}}{dt} = k_{p1L} \frac{d\xi_{1L}}{dt} + k_{i1L} \xi_{1L} + \frac{i_{oL}}{1-D_L} - i_{LL} \end{cases} \quad (A6)$$

The small signal dynamic models of (A5) and (A6) can be calculated by (A7) and (A8), respectively

$$\Delta \dot{\mathbf{x}}_{2H} = \mathbf{A}_{2H} \Delta \mathbf{x}_{1H} + \mathbf{B}_{2H} \Delta \mathbf{x}_{2H} + \mathbf{C}_{2H} \Delta i_{oH} \quad (A7)$$

$$\Delta \dot{\mathbf{x}}_{2L} = \mathbf{A}_{2L} \Delta \mathbf{x}_{1L} + \mathbf{B}_{2L} \Delta \mathbf{x}_{2L} + \mathbf{C}_{2H} \Delta i_{oL} \quad (A8)$$

where

$$\Delta \mathbf{x}_{2H} = [\Delta \xi_{1H} \quad \Delta \xi_{2H} \quad \Delta \xi_{3H}]^T$$

$$\Delta \mathbf{x}_{2L} = [\Delta \xi_{1L} \quad \Delta \xi_{2L}]^T$$

$$\mathbf{A}_{2H} = \begin{bmatrix} nI_{oH} & 0 \\ -1 & 0 \\ -k_{p1H} & -1 \end{bmatrix}, \quad \mathbf{A}_{2L} = \begin{bmatrix} -(mI_{oL} + 1) & 0 \\ -(mI_{oL} + 1)k_{p1L} & -1 \end{bmatrix}$$

$$\mathbf{B}_{2H} = \begin{bmatrix} 0 & 0 & 0 \\ -1 & 0 & 0 \\ -k_{p1H} & k_{i1H} & 0 \end{bmatrix}, \quad \mathbf{B}_{2L} = \begin{bmatrix} 0 & 0 \\ k_{i1L} & 0 \end{bmatrix}$$

$$\mathbf{C}_{2H} = \begin{bmatrix} nV_{oH} \\ 0 \\ 1/(1-D_H) \end{bmatrix}, \quad \mathbf{C}_{2L} = \begin{bmatrix} -mV_{oL} \\ -(mV_{oL}k_{p1L} - 1) \end{bmatrix}.$$

The duty cycle generated by controllers can be viewed as the input signals of the converter models, and determined by the following equations:

$$\Delta d_H = \mathbf{A}_{21H} \Delta \mathbf{x}_{1H} + \mathbf{B}_{21H} \Delta \mathbf{x}_{2H} + \mathbf{C}_{21H} \Delta i_{oH} \quad (A9)$$

$$\Delta d_L = \mathbf{A}_{21L} \Delta \mathbf{x}_{1L} + \mathbf{B}_{21L} \Delta \mathbf{x}_{2L} + \mathbf{C}_{21L} \Delta i_{oL} \quad (A10)$$

where

$$\mathbf{A}_{21H} = [-k_{p1H}k_{p2H} \quad -k_{p2H}]$$

$$\mathbf{A}_{21L} = [-(mI_{oL} + 1)k_{p1L}k_{p2L} \quad -k_{p2L}]$$

$$\mathbf{B}_{21H} = [-k_{p1H}k_{p2H} \quad k_{i1H}k_{p2H} \quad k_{i2H}]$$

$$\mathbf{B}_{21L} = [k_{i1L}k_{p2L} \quad k_{i2L}]$$

$$\mathbf{C}_{21H} = [k_{p2H}/(1-D_H)]$$

$$\mathbf{C}_{21L} = [-(mV_{oL}k_{p1L} - 1)k_{p2L}/(1-D_L)].$$

Substituting (A9) into (A3), and combining with (A7), the model of the converter interfaced with  $ES_H$  can be written as

$$\Delta \dot{\mathbf{X}}_H = \mathbf{A}_H \Delta \mathbf{X}_H + \mathbf{B}_H \Delta i_{oH} \quad (A11)$$

where

$$\Delta \mathbf{X}_H = [\Delta \mathbf{x}_{1H} \quad \Delta \mathbf{x}_{2H}]^T$$

$$\mathbf{A}_H = \begin{bmatrix} \mathbf{A}_{1H} + \mathbf{B}_{1H} \mathbf{A}_{21H} & \mathbf{B}_{1H} \mathbf{B}_{21H} \\ \mathbf{A}_{2H} & \mathbf{B}_{2H} \end{bmatrix}_{5 \times 5}$$

$$\mathbf{B}_H = \begin{bmatrix} \mathbf{C}_{1H} + \mathbf{B}_{1H} \mathbf{C}_{21H} \\ \mathbf{C}_{2H} \end{bmatrix}_{5 \times 1}.$$

By the same token, the small signal model of  $ES_L$  converter can be described by (A12)

$$\Delta \dot{\mathbf{X}}_L = \mathbf{A}_L \Delta \mathbf{X}_L + \mathbf{B}_L \Delta i_{oL} \quad (A12)$$

where

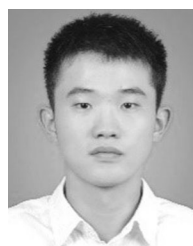
$$\Delta \mathbf{X}_L = [\Delta \mathbf{x}_{1L} \quad \Delta \mathbf{x}_{2L}]^T$$

$$\mathbf{A}_L = \begin{bmatrix} \mathbf{A}_{1L} + \mathbf{B}_{1L} \mathbf{A}_{21L} & \mathbf{B}_{1L} \mathbf{B}_{21L} \\ \mathbf{A}_{2L} & \mathbf{B}_{2L} \end{bmatrix}_{4 \times 4}$$

$$\mathbf{B}_L = \begin{bmatrix} \mathbf{C}_{1L} + \mathbf{B}_{1L} \mathbf{C}_{21L} \\ \mathbf{C}_{2L} \end{bmatrix}_{4 \times 1}$$

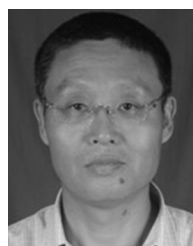
## REFERENCES

- [1] F. Blaabjerg, R. Teodorescu, M. Liserre, and A. V. Timbus, "Overview of control and grid synchronization for distributed power generation systems," *IEEE Trans. Ind. Electron.*, vol. 53, no. 5, pp. 1398–1409, Oct. 2006.
- [2] J. Chi, P. Wang, J. Xiao, Y. Tang, and F. H. Choo, "Implementation of hierarchical control in DC microgrids," *IEEE Trans. Ind. Electron.*, vol. 61, no. 8, pp. 4032–4042, Aug. 2014.
- [3] C. L. Sulzberger, "Triumph of AC—From Pearl Street to Niagara Carl," *IEEE Power Energy Mag.*, vol. 99, no. 3, pp. 64–67, Jun. 2003.
- [4] C. L. Sulzberger, "Triumph of AC. 2. The battle of the currents," *IEEE Power Energy Mag.*, vol. 1, no. 4, pp. 70–73, Jul./Aug. 2003.
- [5] J. Xiao, P. Wang, and L. Setyawan, "Multilevel energy management system for hybridization of energy storages in DC microgrids," *IEEE Trans. Smart Grid*, vol. 7, no. 2, pp. 847–856, Mar. 2016.
- [6] I. Chotia and S. Chowdhury, "Battery storage and hybrid battery supercapacitor storage systems: A comparative critical review," in *Proc. 2015 IEEE Innov. Smart Grid Technol. Asia*, 2016, pp. 1–6.
- [7] A. Kuperman and I. Aharon, "Battery-ultracapacitor hybrids for pulsed current loads: A review," *Renew. Sustain. Energy Rev.*, vol. 15, no. 2, pp. 981–992, 2011.
- [8] H. Liu, Z. Wang, J. Cheng, and D. Maly, "Improvement on the cold cranking capacity of commercial vehicle by using supercapacitor and lead-acid battery hybrid," *IEEE Trans. Veh. Technol.*, vol. 58, no. 3, pp. 1097–1105, Mar. 2009.
- [9] J. Jia, G. Wang, Y. T. Cham, Y. Wang, and M. Han, "Electrical characteristic study of a hybrid PEMFC and ultracapacitor system," *IEEE Trans. Ind. Electron.*, vol. 57, no. 6, pp. 1945–1953, Jun. 2010.
- [10] Y. Yu, Q. Wang, C. Hu, and B. Wang, "The feasibility and superiority of super-capacitors on mild hybrid electric vehicle," in *Proc. IEEE Int. Conf. Mechatronics Autom.*, 2009, pp. 1347–1351.
- [11] L. Gao, R. A. Dougal, and S. Liu, "Power enhancement of an actively controlled battery / ultracapacitor hybrid power enhancement of an actively controlled battery/ultracapacitor hybrid," *IEEE Trans. Power Electron.*, vol. 20, no. 1, pp. 236–243, Jan. 2005.
- [12] Amin, R. T. Bambang, A. S. Rohman, C. J. Dronkers, R. Ortega, and A. Sasongko, "Energy management of fuel cell/battery/supercapacitor hybrid power sources using model predictive control," *IEEE Trans. Ind. Inform.*, vol. 10, no. 4, pp. 1992–2002, Nov. 2014.
- [13] N. R. Tummuru, M. K. Mishra, and S. Srinivas, "Dynamic energy management of renewable grid integrated hybrid energy storage system," *IEEE Trans. Ind. Electron.*, vol. 62, no. 12, pp. 7728–7737, Dec. 2015.
- [14] M. Zeraati, M. E. Hamedani Golshan, and J. Guerrero, "Distributed control of battery energy storage systems for voltage regulation in distribution networks with high PV penetration," *IEEE Trans. Smart Grid*, to be published, doi: 10.1109/TSG.2016.2636217.
- [15] R. Olfati-Saber, J. A. Fax, and R. M. Murray, "Consensus and cooperation in networked multi-agent systems," *Proc. IEEE*, vol. 95, no. 1, pp. 215–233, Jan. 2007.
- [16] R. Olfati-Saber and R. M. Murray, "Consensus problems in networks of agents with switching topology and time-delays," *IEEE Trans. Automat. Contr.*, vol. 49, no. 9, pp. 1520–1533, Sep. 2004.
- [17] J. Schönberger, R. Duke, and S. D. Round, "DC-bus signaling: A distributed control strategy for a hybrid renewable nanogrid," *IEEE Trans. Ind. Electron.*, vol. 53, no. 5, pp. 1453–1460, Oct. 2006.
- [18] K. Sun, L. Zhang, Y. Xing, and J. M. Guerrero, "A distributed control strategy based on DC bus signaling for modular photovoltaic generation systems with battery energy storage," *IEEE Trans. Power Electron.*, vol. 26, no. 10, pp. 3032–3045, Oct. 2011.
- [19] Y. Gu, W. Li, and X. He, "Frequency-coordinating virtual impedance for autonomous power management of DC microgrid," *IEEE Trans. Power Electron.*, vol. 30, no. 4, pp. 2328–2337, Apr. 2015.
- [20] T. Dragicevic, J. M. Guerrero, J. C. Vasquez, and D. Skrlec, "Supervisory control of an adaptive-droop regulated DC microgrid with battery management capability," *IEEE Trans. Power Electron.*, vol. 29, no. 2, pp. 695–706, Feb. 2014.
- [21] P. Magne, D. Marx, B. Nahid-Mobarakkeh, and S. Pierfederici, "Large-signal stabilization of a DC-link supplying a constant power load using a virtual capacitor: Impact on the domain of attraction," *IEEE Trans. Ind. Appl.*, vol. 48, no. 3, pp. 878–887, May 2012.
- [22] P. Wang, C. Jin, D. Zhu, Y. Tang, P. C. Loh, and F. H. Choo, "Distributed control for autonomous operation of a three-port AC/DC/DS hybrid microgrid," *IEEE Trans. Ind. Electron.*, vol. 62, no. 2, pp. 1279–1290, Feb. 2015.
- [23] T. Dragicevic, X. Lu, J. C. Vasquez, and J. M. Guerrero, "DC microgrids—Part I: A review of control strategies and stabilization techniques," *IEEE Trans. Power Electron.*, vol. 31, no. 7, pp. 4876–4891, Jul. 2016.
- [24] A. Riccobono and E. Santi, "Comprehensive review of stability criteria for DC power distribution systems," *IEEE Trans. Ind. Appl.*, vol. 50, no. 5, pp. 3525–3535, Sep./Oct. 2014.
- [25] J. Nazarzadeh and M. J. Jafarian, "Applying bilinear time-optimal control system in boost converters," *IET Power Electron.*, vol. 7, no. 4, pp. 850–860, 2014.
- [26] J. Xiao, P. Wang, and L. Setyawan, "Implementation of multiple-slack-terminal DC microgrids for smooth transitions between grid-tied and islanded states," *IEEE Trans. Smart Grid*, vol. 7, no. 1, pp. 273–281, Jan. 2016.



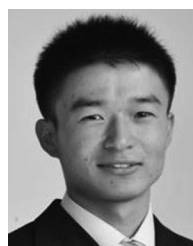
**Pengfeng Lin** (S'16) received the B.S. and M.S. degrees in electrical engineering from Southwest Jiaotong University, Chengdu, China, in 2013 and 2015, respectively. He is currently working toward to Ph.D. degree in electrical engineering in the Interdisciplinary Graduate School, Energy Research Institute, Nanyang Technological University, Singapore.

His research interests include energy storage systems and hybrid ac/dc microgrids.



**Peng Wang** (M'00–SM'11) received the B.Sc. degree from Xian Jiaotong University, Xi'an, China, in 1978, the M.Sc. degree from Taiyuan University of Technology, Taiyuan, China, in 1987, and the M.Sc. and Ph.D. degrees from the University of Saskatchewan, Saskatoon, SK, Canada, in 1995 and 1998, respectively, all in electrical engineering.

He is currently a Professor at Nanyang Technological University, Singapore.



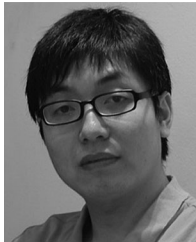
**Jianfang Xiao** (S'11–M'16) received the B.Sc. degree (with first-class Hons.) in mechanical engineering from the School of Mechanical and Aerospace Engineering, Nanyang Technological University (NTU), in 2011, and the Ph.D. degree in electrical engineering from the School of Electrical and Electronic Engineering, NTU, in 2015.

He is currently a Research Fellow in the Energy Research Institute@NTU.



**Junjun Wang** (S'15) received the B.Eng. (first-class Hons.) degree in electrical engineering from Nanyang Technological University, Singapore in 2015.

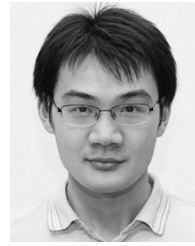
He is currently a Research Staff, Nanyang Technological University. His research interests include hybrid ac/dc microgrid and bidirectional interlinking converter control.



**Chi Jin** received the B.Sc. degree in electrical engineering from Wuhan University, Wuhan, China, in 2007, and the M.Sc. and Ph.D. degrees both in electrical engineering from the School of Electrical and Electronic Engineering, Nanyang Technological University, Singapore, in 2008 and 2013, respectively.

In 2011, he was a Visiting Scholar in the Institute of Energy Technology, Aalborg University, Aalborg East, Denmark, where he worked on the control strategies of hybrid ac/dc/storage microgrid system. Since 2013, he has been in the Energy Research

Institute, Nanyang Technological University, Singapore as a Research Fellow.



**Yi Tang** (S'10–M'14) received the B.Eng. degree in electrical engineering from Wuhan University, Wuhan, China, in 2007, and the M.Sc. and Ph.D. degrees both in electrical engineering from the School of Electrical and Electronic Engineering, Nanyang Technological University, Singapore, in 2008 and 2011, respectively.

From 2011 to 2013, he was a Senior Application Engineer in Infineon Technologies Asia Pacific, Singapore. From 2013 to 2015, he was a Postdoctoral Research Fellow at Aalborg University, Aalborg, Denmark. Since March 2015, he has been at Nanyang Technological University (NTU), Singapore, as an Assistant Professor. He is the Cluster Director of the Advanced Power Electronics Research Program in the Energy Research Institute@NTU.

Dr. Tang is an Associate Editor of the IEEE JOURNAL OF EMERGING AND SELECTED TOPICS IN POWER ELECTRONICS. He received the Infineon Top Inventor Award in 2012 and the Early Career Teaching Excellence Award in 2017.